	MART-GEN-UG	v2.0
	ART-XC – Mission User's Guide	March 27, 2023

ART-XC – Mission User's Guide

Prepared by: MSFC/ST12 ART-XC Team
NASA, Marshall Space Flight Center

March 27, 2023

Abstract

This document provides a description of the *Astronomical Röntgen Telescope - X-ray Concentrator* (ART-XC) instrument on board the Spectrum-Röntgen-Gamma (SRG) high-energy astrophysics observatory. The purpose of this document is to provide data end users of ART-XC with the information necessary to understand how the instrument operates including general specifications, available observing modes, and performance parameters.

Revision History

Revision	Author	Date	Change
v1.0	D.Swartz/USRA	06/11/2021	Initial Draft
v2.0	MART team	09/14/2021	Working Draft

Contents

1 Introduction

1.1 Purpose

This document provides an overview of the *Astronomical Röntgen Telescope - X-ray Concentrator* (ART-XC) X-ray instrument aboard the Spectrum-Röntgen-Gamma (SRG) high-energy astrophysics observatory. Its purpose is to provide the data end user relevant information needed to understand how the instrument is configured, how it operates, and how it performs.

1.2 Scope

This document is intended as a usage guide for ART-XC data end users. This document applies to all phases of the ART-XC mission including the calibration phase which commenced c. August 2019, the all-sky survey phase that began in December 2019 and is planned to continue through December 2023 (with final public data delivery c. March 2025) and the planned pointed phase following after the all-sky survey and continuing to the end of mission.

1.3 Change Authority/Responsibility

The NASA Office of Primary Responsibility for this document is the MSFC ART-XC team Principal Investigator.

1.4 Applicable Documents

Publicly-accessible literature is cited throughout this document and a full bibliography is provided. In addition, the following documents are relevant:

Data Dictionary	MART-SW-SDD-V01
Calibration Database	MART-CAL-CALDB-V00
Ground Calibration Report	MART-CAL-CdTe-V02
PSF and Vignetting Guide	MART-VIG-PSF-V00
Event Energy Computation	MART-GAIN-D29-V00
Software Guide	MART-SW-SWGUIDE-V01
FITS format	https://heasarc.gsfc.nasa.gov/docs/heasarc/fits.html
CALDB files	https://heasarc.gsfc.nasa.gov/docs/heasarc/caldb/caldb_intro.html

2 Mission Overview

ART-XC, the *Astronomical Röntgen Telescope - X-ray Concentrator*, is one of two instruments aboard the Spectrum-Röntgen-Gamma (SRG; aka Spektr-RG) high-energy astrophysics observatory. SRG is a joint Russian – German mission launched from the Baikonur, Kazakhstan, Cosmodrome 13 July 2019 into a halo orbit about the Sun-Earth L2 Lagrange point. Following a Performance Verification and Calibration phase en route to its final orbit, SRG began a 4-year all-sky survey on 13 Dec 2019. At the conclusion of the all-sky survey phase, SRG is planned to carry out 2.5 years of pointed observations of targets of interest.

The SRG mission is operated by the developer of the spacecraft bus, the Lavochkin Research and Production Association, via daily ground contacts through the Russian Centers of Deep Space Communications. The Russian Space Research Institute (IKI) SRG Science Data and Operations Center in Moscow processes the telemetered data to produce Level 1 event lists, housekeeping, and spacecraft attitude files. This data are retrieved by Marshall Space Flight Center (MSFC), Huntsville, AL, from IKI via a secure file transfer protocol and further processed.

Final Level 2 data products, data processing and reduction software, and an ART-XC-specific calibration database (CALDB) are delivered for long term archiving and public dissemination by MSFC to the

High Energy Astrophysics Science Archive Research Center (HEASARC) at the Goddard Space Flight Center (GSFC) in Greenbelt, MD. All data and products conform to the Office of General Investigator Programs (OGIP) standards for format and content.

Funding for the US participation in data processing, archiving, and access by the public is provided by the Astrophysics Division of the NASA's Science Mission Directorate.

All data obtained by the ART-XC telescope are the property of the Russian Space Research Institute. In exchange for the delivery of a subset of the ART-XC X-ray mirror modules, MSFC shares with IKI rights to data within a 200 deg^2 area around the North Ecliptic Pole (where the sensitivity of the all-sky survey reaches its maximum). Negotiations to deliver the ART-XC all sky survey data in its entirety through the HEASARC are ongoing.
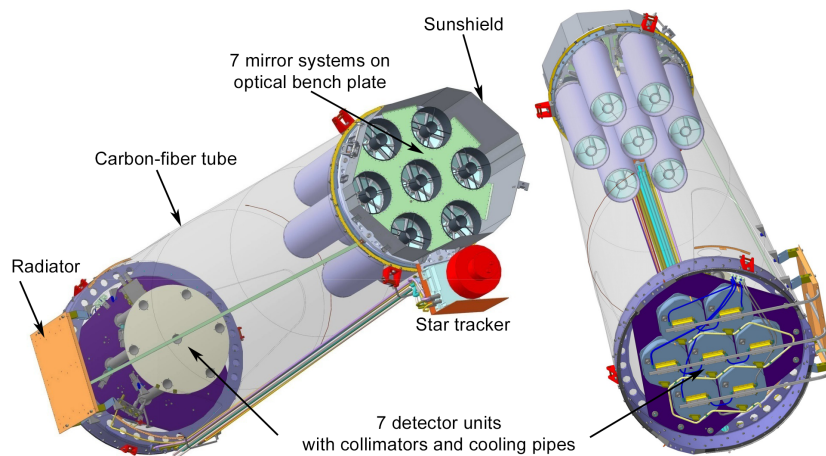
3   The ART-XC Instrument Overview

Figure 1:   Schematic of ART-XC instrument showing the array of 7 co-aligned mirror modules, sunshield, and star tracking camera at one end of the carbon-fiber optical bench and the matching array of 7 detectors, collimators and passive thermal control at the other end of the optical bench.

The ART-XC payload is a focussing X-ray instrument consisting of seven nearly identical and co-aligned telescopes (Figure 1) each comprised of a mirror module assembly focussing X-ray photons onto a double-sided strip CdTe detector capable of registering the position, energy, and arrival time of events over a ~ 0.3 deg^2 field-of-view. ART-XC telescopes operate in the 4 to 30 keV X-ray band though the detectors are sensitive to above ~ 100 keV. The instrument attitude is monitored by up to three star trackers and an inertial navigation system (gyroscopes) that allow for reconstructing the celestial locations of each registered event. Table 1 lists the ART-XC performance parameters.

3.1   Mirror Module Assemblies

NASA's Marshall Space Flight Center designed, fabricated and calibrated the X-ray mirror module assemblies (MMAs) also referred to in the literature as mirror systems (MSs). Each module consists of 28 nested, co-aligned, Wolter-I double-reflection grazing incidence mirror shells made of a Ni-Co alloy in an electroformed replication process (Gubarev et al., 2012, 2014). Each shell is coated with 10 nm Ir at 90% bulk density. The assembly is mounted to a spider at the incidence end and has a thin aluminized Mylar film over the entrance aperture to aid thermal control of the mirrors.

Each MMA has an effective area ~ 65 cm^2 at $4-8$ keV decreasing at and above the Ir M-edges ($\sim 10-13$ keV) with very little reflection above 30 keV. The on-axis measured MMA half-power diameter (HPD) is $30''$ to $35''$. The telescopes are defocused by -7 mm from the nominal 2700 mm focal length of the

Table 1: ART-XC SYSTEM PERFORMANCE[†]

Mirror Modules	nested, grazing incidence, Ir-coated, Ni/Co alloy
Effective Area	450 cm^2 at 8 keV on-axis (7 modules)
Half-Power Diameter	30″ on-axis
Detectors	1 mm thick CdTe Schottky Diode double-sided strip
Energy Resolution	9% at 14 keV
Quantum Efficiency	50% at 4.6 keV, 85% at 8 keV
Time Resolution	23 μs
Entrance Window	100 μm Be
System	
Effective Area	385 cm^2 at 8 keV on-axis (7 modules)
Energy Range	4-30 keV
Focal Length	2.7 m (defocussed to 2.693 m)
Field of View	36′ (48x48 595μm-wide strips)
Spatial Resolution	45″ on-axis HPD

[†]See Pavlinsky et al. (2018) for complete specifications.

MMAs in order to optimize the angular resolution out to ∼10′ radius before expanding to ∼2.5′ at the edge of the detector field-of-view (FOV).

3.2   Focal Plane Detectors

The Russian Space Research Institute developed the focal plane X-ray detectors. The detectors are often referred to in the literature as 'units of roentgen detectors' or URDs. They are built from CdTe crystal dies manufactured by Acrorad (Japan) each matched to two VA64TA1 ASICs manufactured by Ideas (Norway) to service the top and bottom electrodes in a double-sided strip configuration. Each CdTe crystal is 29.95×29.95×1.00 mm with 48 parallel Au-over-Pt electrode strips on the top and 48 Al/Ti/Au electrode strips on the bottom patterned by photolithography. Each electrode strip is 520 μm wide with a 75 μm gap between strips. The top strips are oriented perpendicular to the bottom strips to allow for two-dimensional reconstruction of events in the detector plane.

The resulting 'pixel' size is ∼45″ at the 2693 mm focal length and the FOV is ∼36×36′ although additional structures (e.g., cylindrical collimators, see § 8) decrease this value slightly. The normal operating mode is to record the signal (PHA) registered in the top and bottom strips where the event was triggered along with the four (two top and two bottom) adjacent strips. The event energy is then determined by a weighted combination of these six PHA values in ground processing. The detectors operate in the ≳4 keV energy range. The effective quantum efficiency, accounting for a thin Be window, top electrodes, and the thin aluminized mylar thermal barrier on the MMAs, is ∼50% at 4.5 keV improving to ∼85% at 8 keV.

Each detector housing contains a retractable radioactive ^{55}Fe + ^{241}Am calibration source used to monitor gain and energy resolution.

3.3   Star Cameras

A star tracking camera, referred to by the Russian acronym as the BOKZ-MF[1], is mounted next to the ART-XC MMAs (Figure 1) and is aligned with the system's optical axis. The star tracker provides attitude information supplemental to the navigation system of gyroscopes. There are also two star trackers mounted on the eROSITA optical bench whose output is also provided as part of the ART-XC data products. BOKZ-MF has a 14° FOV, can track stars as faint as 6th magnitude, and has an accuracy $\sigma_x, \sigma_y/\sigma_z = 2.5/25″$ (rms). The star tracker attitude data, in the form of an orientation matrix, is sampled at a rate of 1 Hz.

---

[1]Block for Determining the Coordinates of the Stars

4   Spacecraft Orientation and Orbit

The ART-XC spacecraft coordinate system is shown in Figure 2. The $+X$ axis is defined to be the line from the center of the detector plane to the centers of the mirror module array. The $+Z$ axis is along the nominal direction toward the Earth and Sun. In order to maintain power to the solar arrays, the angle between the spacecraft $+Z$ axis and the spacecraft-to-Sun line is restricted to not exceed $13°$. Similarly, the angle between the Z axis and the spacecraft-to-Earth line cannot exceed $24°$ for proper alignment of the medium gain antenna.
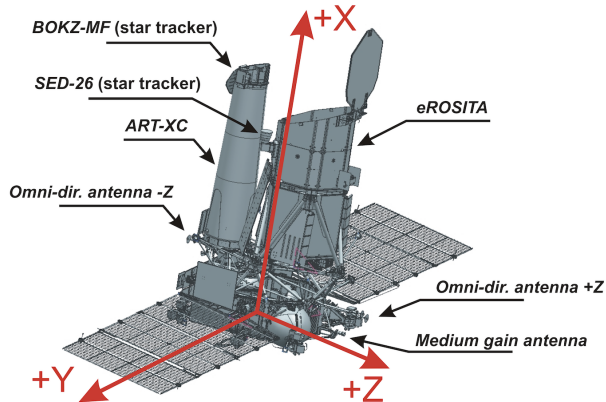

Figure 2: Schematic of SRG mission indicating major components related to the ART-XC instrument including locations of star tracking cameras and communication antennae. The spacecraft coordinate system is also shown with $+X$ parallel to the telescope optical axis from the detector/focal plane toward the mirror modules, the $+Z$ axis in the nominal direction toward the Earth and Sun, and the $+Y$ axis along the length of the solar arrays. Note the solar arrays are not shown in the correct orientation in this schematic: They should lie in the X, Y plane rather than the Y, Z plane.

SRG operates in a halo orbit around the Sun-Earth L2 Lagrange point. Figure 3 shows the path of SRG in the ecliptic plane from launch in July 2019 through the completion (Dec 2020) of the six-month Epoch 2 portion of the all-sky survey phase. Note the radius of the orbit around L2 is of order 750,000 km and the orbital period is of order 6 months.
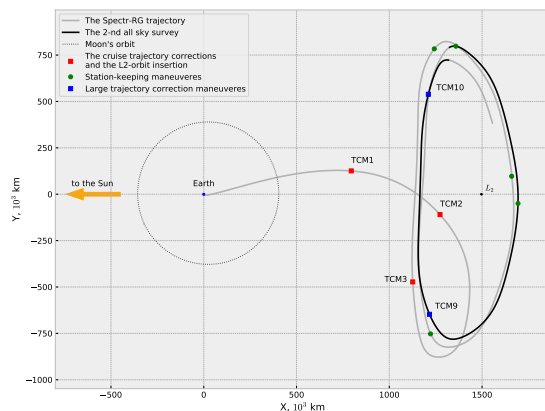
Figure 3: Projection of the path of SRG from launch through the end of the first year (2 Epochs, see § 5.1) onto the ecliptic plane. (Coordinate labels in this figure should not be confused with the spacecraft coordinates.)

5   Observing Modes

5.1   Survey Mode

The primary SRG observing mode is Survey Mode used to execute a four-year-long all-sky survey that began in December 2019. The all-sky survey is designed to image the entire sky every six months. This is accomplished by rotating the spacecraft about the Z-axis (§ 4) which remains nearly parallel to the

Sun-Earth axis (with the optical (X-)axis aligned 90° from the rotation axis). In this way, the rotation axis shifts by approximately one degree per day, or $10'$ per rotation, as SRG follows the motion of the Earth around the Sun. The rotation rate is $1.5°$ min^{-1} or one complete rotation every 4 hours. The full FOV of ART-XC is $36'$, so that a celestial source near the ecliptic plane is exposed for ∼20 seconds 6 times in succession only once every 6 months. Sources near the ecliptic poles are observed much more frequently, up to 120 s per day year round. ART-XC will image the entire sky eight times in four years. Each complete survey is referred to as an 'Epoch;' there are thus 8 epochs planned for the all-sky survey.

The rotation axis shift rate varies because of the elongation in the ecliptic plane of the SRG halo orbit and because of restrictions on the orientation of the spacecraft (§ 4) relative to the Earth. Specifically, SRG moves ahead of Earth for 3 months and lags Earth for the next 3 months which causes variations of the drifting rate of the scanning plane. This 'z-speed' varies from 0.7 deg/day at the nearest to Earth segment of the orbit up to 1.6 deg/day at its farthest segment. Note that variation of the Z axis speed causes variations of exposure of the sky; higher speed leads to lower exposures while lower speed allows higher exposures of the corresponding sky regions. A complete timeline of z-speed variations is maintained at the IKI site https://plan.srg.cosmos.ru/monthplan/, see also Sunyaev et al. (2021) for a graphical representation of the z-speed over the first two survey epochs. The survey pole has remained at R.A. 270.0, Decl. 66.560708889 (J2000) during the first 3 epochs of the all-sky survey but may be changed slightly as the mission progresses.

5.2   Pointed & Scan Modes

The optical axis of the telescope is fixed in a given direction in pointed mode. In scan mode, the spacecraft conducts a series of repeated consecutive rotations around the Y and Z spacecraft axes which enables observations of regions of the sky as large as $12.5° \times 12.5°$ with uniform exposure.

The pointed and scan modes were used exclusively during the Calibration and Performance Verification phase of the mission that took place while SRG was enroute to Sun-Earth L2. These modes are also used occasionally during the all-sky survey phase to perform special calibration observations, during orbit corrections, and for target of opportunity observations of transient objects at the discretion of the IKI Science Data and Operations Center. A complete mission timeline is maintained at the IKI planning page https://plan.srg.cosmos.ru/.

Another operational 'mode' can also be commanded. This mode is used to insert the on-board calibration source into the FOV of a detector. This mode is used for only one detector at a time. Details are given in § 8.4.1.

6   Operations & Data Pipeline

This section briefly describes the fundamental on-orbit and ground support operations necessary to conduct the ART-XC science program.

6.1   Mission Planning

Mission planning for a calendar month is initiated at the science operations center at IKI using inputs from the ART-XC and eROSITA science teams and predictions of the SRG trajectory provided by the mission operations center (MOC) operated by Lavochkin Association (also referred to as NPO Lavochkin or NPOL). The MOC also provides preliminary ground contact scheduling and the schedule for any critical operations such as trajectory corrections. The monthly schedule specifies targets, observing modes (including on-board calibration source insertions), hardware settings (such as URD high voltage settings for depolarization routines), exposure times, etc. Once this mid-term plan has been verified consistent within operational constraints, daily schedule blocks are prepared detailing the sequence of commands for ground stations, the spacecraft, and the instruments. The command sequence for the spacecraft and scientific instruments may be executed in real time during the ground contact session or stored in the onboard control system memory for execution at specified times from the beginning of a session until at least the beginning of the next contact session. Note this naturally sets the minimum SRG response time to transient events to the time between ground contact sessions.

6.2   Ground Operations

Communication between SRG and the ground is provided through the Russian Deep Space Network 64 m TNA-1500 antenna at Bear Lakes, the 70 m P-2500 antenna at Ussuriysk and, if necessary, the 12 m TNA-57 antenna located at Baikonur. Ground contacts are executed daily. Ground contact sessions last approximately 4–5 hours during which daily accumulations of science and housekeeping data is downlinked, trajectory measurements are conducted, the status of onboard systems and scientific instruments is monitored, and the time-tagged command sequence for a subsequent period of up to several days is uplinked. The contact sessions are conducted by the MOC with all telemetry transmitted to IKI's science operations and data center in near real-time.

The science operation center monitors the health and physical state of the telescope hardware (temperatures, current and voltage levels, etc.), verifies telemetry for transmission errors, decommutates the data stream into housekeeping, detector, and star tracker units, and performs preliminary processing of the science data (including generating quick-look data products). The typical volume of ART-XC data is 90 to 120 MB per day. The IKI science data center then performs data reduction and archiving among other tasks. Data reduction includes converting raw telemetry data from binary format to FITS format (Level 0 processing), calibrating (Level 1) and cleaning (Level 2) the science data.

6.3   Data Reduction

Level 1 data products include separate event lists for each of the seven telescopes and a spacecraft attitude file. For survey mode observations (5.1), a separate Level 1 event list FITS file is constructed for each sky 'tile' (and for each telescope) containing events. For pointed and scan mode observations, these event list files span the entire time of the observation. In Level 1 processing, for each event, the event energy is calibrated from the PHA values, a time-of-arrival correction is applied, approximate sky coordinates are calculated, and an event GRADE is assigned.

In Level 2 processing performed at MSFC, an improved aspect solution is computed and applied to determine sky coordinates for each event, pulse invariant (PI) values are assigned, intervals of high background flaring are identified and logical FLARE values assigned, and a FLAG value indicating where on the detector the event occurred is updated.[2] In addition, the data is cleaned of certain events such as those with unphysical energies, detector coordinates, etc. The aspect solution requires spacecraft attitude reconstruction which is provided by orientation data from the star trackers, coupled with the gyroscopic angular velocity sensor data, resulting in an orientation quaternion determination. See § 9 for details.

7   Mirror Module Assemblies (MMAs)

7.1   Physical Configuration

The seven ART-XC MMAs (plus one flight spare) each consist of 28 thin, nested, co-aligned and co-axial grazing-incidence reflective optics (or shells) following the Wolter-I prescription. Individual shells were fabricated by electroforming a Ni/Co alloy onto a figured and superpolished aluminum mandrel from which they are later released by differential thermal contraction. The shells are monolithic in that they combine the full azimuthal range of both the paraboloid and hyperboloid reflecting surfaces. This construction increases rigidity which improves angular resolution of the thin, lightweight shells. The shells vary in thickness from 250 μm (inner) to 350 μm (outer) and range in diameter from about 50 mm to 150 mm. The total length of each optic is 580 mm. The shells are coated with 10 nm of 90% bulk density Ir to enhance their high-energy reflectivity up to 30 keV.

The individual shells are co-aligned and mounted to a a nine-spoke 'spider' on one end through combs glued onto the spider spokes. Three attachment lugs on the periphery of the spider secure each module to a support plate at the entrance to the optical bench. An 18.5 μm Mylar film with an 0.11 μm Al layer entrance filter is mounted to the entrance window for passive thermal control. Combined

---

[2]FLAG=0, 2, or 3 depending on whether the event occurred in the open area beneath the Be window, in an edge strip, or under the circular Al plate, respectively; see § 8.

with thin aluminum thermal insulator tubes with active heaters surrounding each MMA, the modules are maintained within ± 3 C of the nominal 20 C operational temperature. Figure 4 shows a schematic cut-away of a mirror assembly mounting to a spider. Also shown is the view of the support plate holding the 7 ART-XC MMAs arranged in a hexagon array with the remaining MMA in the center.

The nominal focal length of the MMAs is 2700 mm but they have been purposely defocussed by -7 mm to the optimal intra-focal position to provide a more uniform angular resolution across the ART-XC field of view.
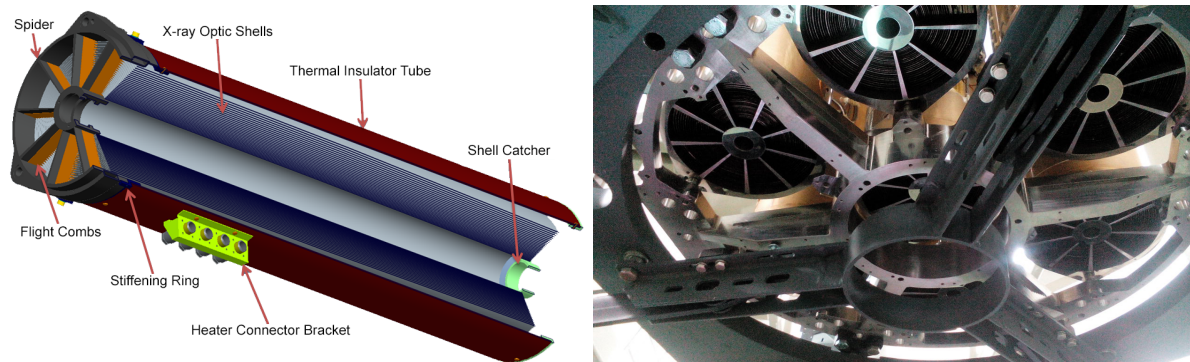

Figure 4: *Left:* Schematic cut-away view of an ART-XC MMA showing the nested mirror shells (gray), the mounting 'spider' located at the X-ray entrance end of the module and related hardware. The MMA is approximately 600 mm long and 175 mm diameter. *Right:* View of the entrance to the optical bench showing the 7 ART-XC MMAs attached to a support plate (and alignment jig!!!) I SAW A CLEANER PICTURE SOMEWHERE BUT CAN"T FIND IT NOW.

7.2   Calibration

Calibration of individual mirrors and of all eight (7 flight and 1 spare) MMAs was performed at MSFC's 100 m Stray Light Test Facility (SLTF) in 2014 as reported in Gubarev et al. (2012) and Gubarev et al. (2014). The flight spare module, MMA6, and the flight spare detector, URD29, were independently tested at IKI's X-ray test facility in 2016-2017 (Pavlinsky et al., 2018) and again at the Panter test facility in Germany in October 2018.

Calibration of the MMAs at MSFC used a Trufocus 50 kV microfocus X-ray source with a Cu target (providing strong emission at the Kα line at $\sim$8 keV), a non-imaging Amptek XR-100T CdTe detector with a 5 mm $\times$ 5 mm entrance aperture, and a high-resolution iKon-L 936 ANDOR CCD camera. The CdTe detector was primarily used for measuring the effective area and encircled energy fraction (including the half-power diameter, HPD) as functions of X-ray energy, E, off-axis (polar) angle, θ, and azimuthal angle, ϕ. The CCD camera was used to image the MMA point spread function (PSF) over a range of θ and ϕ.

Independent calibration measurements of the flight spare MMA and URD were made at the 60-m IKI X-ray test facility in 2016-2017 (Pavlinsky et al., 2018). X-ray sources included Cr, Cu, Mo, and Ag targets. The X-ray flux was monitored using an Amptek XR-100 Si drift detector (SDD) and an XR-100T CdTe detector both with 5 mm $\times$ 5 mm entrance apertures in addition to URD29. Measurements included the system energy-dependent encircled energy fraction.

Additional calibration of the flight spare telescope was performed at the PANTER X-ray test facility of the Max-Plank-Institute for Extraterrestrial Physics in Neuried, Germany in October 2018. These tests also used the PANTER TroPIC pnCCD camera to cross-calibrate the flight spare detector. The TroPIC camera is similar to the eROSITA cameras. It is a 256$\times$256 array of 75μm pitch pixels suitable for moderate spatial resolution imaging. Measurements included the on-axis effective area, the vignetting function at several discrete energies, and the on-axis encircled energy fraction at several energies.

7.3   Performance

7.3.1   On-Axis Effective Area

Figure 5 displays the on-axis effective area of the seven flight MMAs, the combined total effective area, and the effective areas convolved with the flight spare detector quantum efficiency. Note the effective area is highest and nearly constant below the Ir L-edges at $\sim 11-13$ keV (the M-edges of Ir at $\sim 2-3$ keV have only a small effect). When convolved with the efficiency of the detector (Figure 5; right panel), the effective area is reduced at low energies due to the combination of the aluminized Mylar thermal shield at the entrance to the optical bench, the Be entrance window above the detector, and the Au+Pt electrodes on the top of the detector (§ 8).

The mean effective area of the MMAs is 61.7±2.1, 67.1±1.8, 32.4±1.5, and 10.3±0.9 cm^2 at energies 4.0, 8.1, 12.0 and 20.0 keV, respectively. Thus, the total effective area at, say, 8.1 keV for the 7 co-aligned ART-XC flight MMAs is ~ 470 cm^2 while the system (mirrors+detectors) effective area is ~ 385 cm^2.
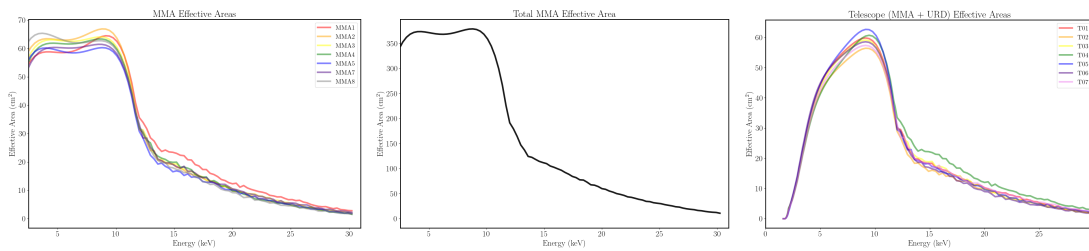

Figure 5:   *Left:* Effective area of the seven flight MMAs as a function of energy as measured at the MSFC SLTF. The data have been smoothed below 12 keV with a 4th-order polynomial fit to the data. *Center:* Combined (total) effective area of all 7 flight mirror modules. *Right:* The effective area of the seven flight MMAs convolved with the efficiency of the flight spare detector.

7.3.2   Off-Axis Effective Area

The off-axis effective area is represented by a vignetting function defined as the ratio of the off-axis effective area as a function of polar angle θ to the on-axis area (at $\theta = 0$). The shape of the vignetting function depends on photon energy; falling more steeply with θ for higher energies (Figure 6). There is no measurable dependence of the off-axis effective area with azimuth for the ART-XC MMAs.
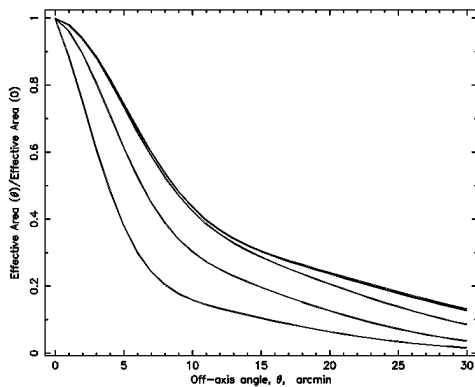

Figure 6:   Azimuthally-averaged effective area as a function of off-axis angle, θ, normalized to the on-axis value, for several representative energies; 4, 6, 8, 12, and 20 keV from top to bottom (the curves for 4 and 6 keV are nearly identical). The averages are over 8 equally-spaced angles, ϕ, spanning the full 360° range of azimuths.

7.3.3 Point Spread Function & Encircled Energy Fraction

A useful parameterization of the MMA point spread function (PSF) is the encircled energy fraction (EEF). This is a two-dimensional integral of the PSF as a function of radius from the image center (peak). The PSF and hence the EEF depend upon off-axis angle, θ and photon energy, E. The PSF broadens, and the EEF decreases, as θ increases because of mirror aberrations and as E increases because of increased X-ray scattering.

Encircled Energy Fraction The left panel of Figure 7 shows the on-axis EEF over a broad range of X-ray energies, E, and the right hand panel shows the EEF at $E = 6.5$ keV for several angles, θ.
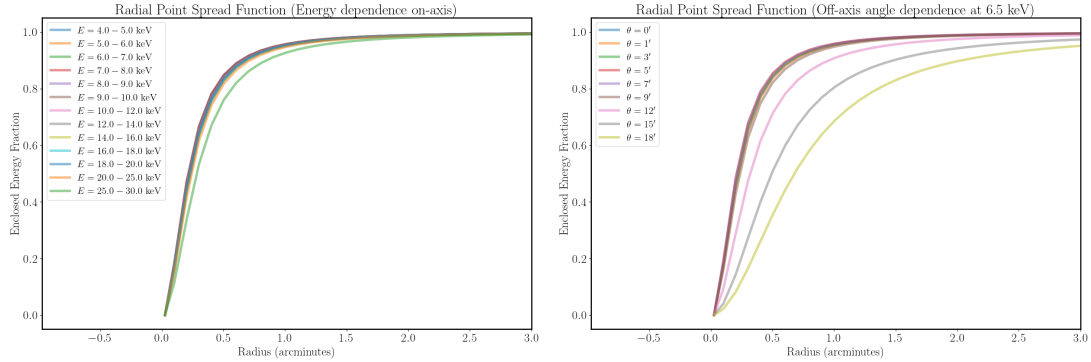

Figure 7: *Left:* The enclosed energy fraction for ART-XC MMA 3 (Telescope 01) as a function of energy for photons on-axis. *Right:*The enclosed energy fraction for ART-XC MMA3 (Telescope 01) as a function of off-axis angle for an incident photon energy of 6.5 keV.

Half-Power Diameter Another useful and commonly-used parameterization of the PSF is the half-power diameter (HPD) defined as the diameter enclosing 50% of the total power; i.e., the HPD corresponds to an EEF of 0.5. HPD is more representative of the actual MMA performance than is the FWHM because the HPD accounts properly for the extended wings of the PSF whereas FWHM characterizes only the (typically narrow) core of the PSF. Figure 8 shows the HPD for on ART-XC flight MMA as a function of θ and E. Note the MMA performance has been optimized for energies below the IR M-edges where the effective area is at maximum. The HPD of the ART-XC MMAs is $<35''$ at energies $E \lesssim 10$ keV within $\sim 12'$ of the optical axis. Note also that the HPD decreases slightly from $\theta = 0$ to $\theta \sim 7'$ as a result of setting the detector plane at a slightly defocussed position (§ 7.1).
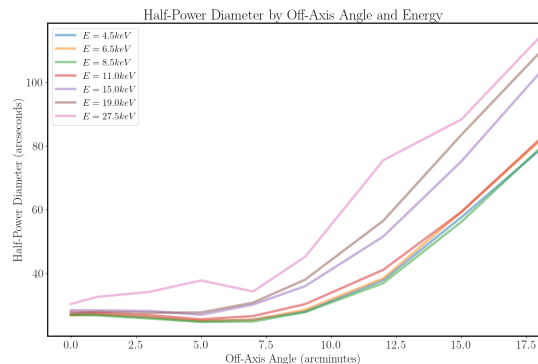

Figure 8: The half-power diameter of ART-XC MMA3 (Telescope 01) as a function of off-axis angle, θ, and energy, E. Note the nearly constant HPD$\lesssim 35''$ at energies $E \lesssim 10$ keV out to $\sim 12'$ of the optical axis due to the slight defocussing of the optical assembly that optimizes the PSF over this broad portion of the FOV.
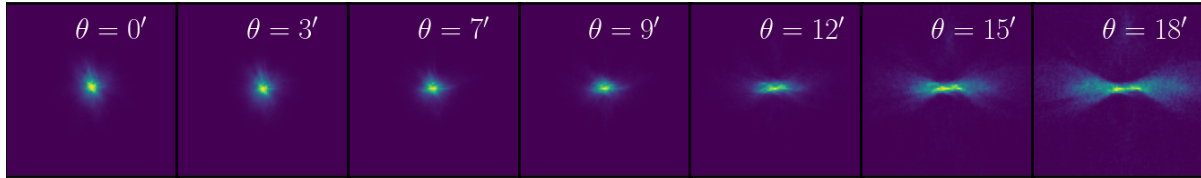
Figure 9: High-resolution images of a point-like source at finite distance taken at MSFC's Stray Light Test Facility at Cu Kα (8 keV) as imaged by MMA3. The off-axis angle of each image is overlaid on the individual panels. Images shown were taken at azimuthal angle $\phi = 0°$ in test chamber coordinates. Thus, the direction towards $\theta = 0$ in each panel is towards the bottom of the page. Although the shape of the PSF is clearly asymmetric, especially at large off-axis angles, the PSF is independent of azimuth.

Point Spread Function   Figure 9 shows a series of high-resolution images of a point source taken at the MSFC SLTF. The images cover polar angles, θ, from $0'$ to $18'$ off-axis. This is one portion of a scan taken over the range $\pm 18'$ at azimuthal angle $\phi = 0°$. The X-ray light source used for these measurements produces Cu Kα and Kβ lines at $\sim$8 keV and 8.9 keV, respectively, and a weak continuum. The images were taken using the ANDOR iKon-L 936 CCD camera with a pixel size of $13.5 \times 13.5 \mu$m corresponding to $1.007''$ at the 7 mm defocussed position appropriate for a finite source distance. (For a nominal focal length of 2700 mm for an object at infinite distance, the principal focus falls at 2772 mm for a source distance of 103.3 m at the SLTF.) All images were binned by 2 giving a final resolution of $\sim 2''$. Figure 9 indicates the size and shape of the angular response remains circular and nearly unchanged within $9'$ of the optical axis before distorting into a bowtie shape at large off-axis angles. The near constancy of the PSF shape for angles $< 9'$ is due to the designed defocus to obtain the optimal focal distance (see Gubarev et al. (2014)).

The CCD images shown in Fig. 9, along with all the others taken in this manner, are contained in the ART-XC CALDB as FITS images.

Krivonos et al. (2017) parameterized the 2-dimensional shape of the PSF within $9'$ of the optical axis as a linear combination of two King profiles, each of the form

$$K(\theta) = \left(1 + \frac{r^2}{\sigma^2}\right)^{-2},$$

where r is the radial distance from the PSF peak (centroid) and θ is the off-axis angle. The characteristic core size, σ_{core}, varies slightly with θ (and MMA) by $\sim$12% about an average of 14.2 (Krivonos et al., 2017). The characteristic size of the wings, on the other hand, is $\sigma_{\text{wing}} \sim 200''$ for $\theta < 5$, increases up to $\sim$400$''$ at $\theta = 5'$ and decreasing again for larger θ. Based on this model, the half power diameter, HPD$<35''$ for $\theta < 7'$ with $<$10% of the encircled energy fraction contained in the wings. These values increase only slightly up to off-axis angles $\theta = 9'$.

This simple model does not describe well the complex asymmetric PSF shape beyond $\theta = 9'$, Krivonos et al. (2017) fit the off-axis PSF to ellipses and tabulated the semi-major and minor axis dimensions as a function of enclosed count fraction (similar to the EEF) for off-axis angles $9 \leq \theta \leq 24'$. The size of the 50% enclosed count fraction varies from $\sim$22$''$ semi-major axis at $\theta = 9'$ up to $\sim$90$''$ at at $\theta = 18'$.

7.3.4   Optical Artifacts

Single-Reflection Ghost Images, spider shadows ,etc.

[[Additional off-axis CCD images (§ **??**) . Stuff from Ron Elsner's ray-tracing; on-orbit Crab image example shows singles and shadows of spokes]]

7.4   Optical Axis and Aimpoints

See section 9.

8   Focal Plane Detectors (URDs)

The focal plane detectors are referred to as 'units of roentgen detectors' (URDs) in the literature.

8.1   Physical Configuration

The X-ray detectors are double sided strip detectors constructed on a 1 mm thick CdTe crystal (Levin et al., 2014). There are 48 parallel electrode strips on both the top and bottom of the crystal. The top strips are oriented perpendicular to the bottom strips to allow for two-dimensional reconstruction of events in the detector plane. The strip electrodes are patterned by photolithography onto the CdTe crystal. In addition, a guard ring is added that surrounds the electrodes. The top electrodes are 100 nm Au over 50 nm Pt. The bottom electrodes are similar thicknesses of Au over Ti over Al. The CdTe/Al on the bottom electrode forms a Schottky barrier to provide a very low leakage current. Each strip is 520 μm wide with 75 μm gaps between electrodes. The guard ring limits the sensitive region to 28.485×28.485 mm (Levin et al., 2014). The resulting 'pixel' size is $\sim$45$''$ and the maximum FOV is 36×36$'$.

Figure 10 shows a CdTe crystal mounted in a ceramic holder along with two ASICs used to read out the top and bottom electrodes.
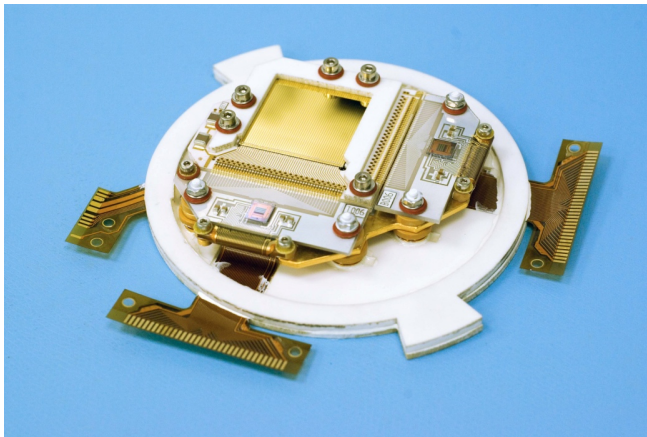

Figure 10:   An ART-XC X-ray detector hybrid integrated circuit showing the CdTe crystal (gold square) held to a 3-layer ceramic mounting structure (white). The two readout ASICs are visible on adjacent edges of the crystal. External connections to the board provided through flexible circuit boards that extend outside the bottom ceramic mounting disk are also visible.

The detector is sealed within a 1 mm thick Al protective cover with a circular entrance window forming the inner sealed housing (Pavlinsky et al., 2018). The entrance window is a 30.05 mm diameter, 100 μm thick, Be plate held 9.5 mm above the CdTe crystal. The window is centered and fixed to a 1.5 mm thick Al ring with inner diameter 32.3 mm. However, as shown in Figure 11, the center of the window is located slightly offset from the center of the crystal (Pavlinsky et al., 2019a). Figure 11 also shows that the corners of the crystal are masked from direct X-radiation although the small annulus between the outer edge of the Be window and the inner edge of the Al ring is only partially opaque at high energies.

The outer diameter of the Al ring is 36 mm. Outside this ring, the inner housing is covered with 1 mm thick layers of Cu and Sn. Just above the window, there is a three-layer Al/Cu/Sn (each 1 mm thick) cylindrical collimator extending above the detector housing. The collimator inner diameter is 32 mm and the height is 70 mm. Mounted to the side of the collimator is a retractable ^{55}Fe + ^{241}Am calibration source (§ 8.4.1).

Transmission through the Be window, Au+Pt top electrodes, and the aluminized Mylar thermal shield atop the MMA mount are the main factors reducing the system effective area at low energies. However, the performance of the detectors themselves limit the useful energy range to >4 keV (§ 8.3).
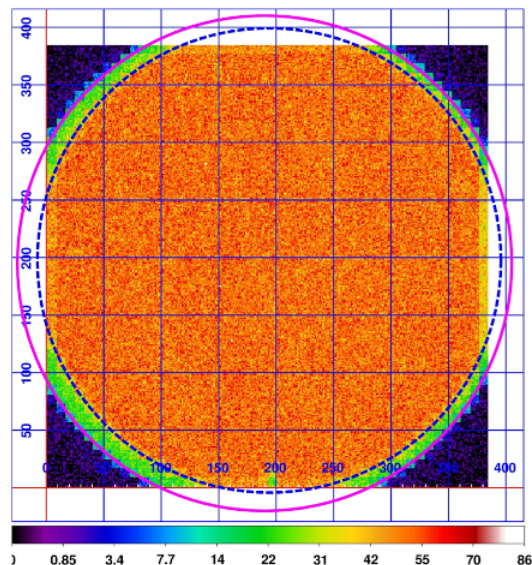
Figure 11: Image of detector illuminated by high energy X-rays rendered at $8\times$ actual resolution to visualize regions of the active detector area masked by the outer edge of the Be window (blue dashed circle) and the inner edge of the Al ring (total thickness 2.5 mm; magenta solid circle). Note also the designed offset of the center of the circular entrance window from the center of the square CdTe crystal.

8.2   Calibration

Calibration of the ART-XC detector units was carried out at IKI and at IKI's 60 m X-ray test facility. Calibration of the detectors at he sub-assembly level is reported in Levin et al. (2014) and includes characterizing the event processing, measurements of the detector polarization rate, sharing of signal between adjacent electrodes, and the spectroscopic and imaging performance of the detectors. Levin et al. (2016) reports the results of thermal-vacuum and vibration testing.

Pavlinsky et al. (2018) describes the results of tests of the flight spare URD29 detector including energy resolution and quantum efficiency using ^{55}Fe + ^{241}Am sources similar to those available on-orbit. Pavlinsky et al. (2019a) reports descriptions of the determination of low-energy thresholds (and subsequent event GRADE distributions; see § 8.1). This report also provided estimates of the (flight spare) detector quantum efficiency through bootstrap comparisons to calibrated Amptek XR-100T-CdTe and XR-100SDD detectors.

Results of the system performance of the flight spare telescope, URD29 + MMA6, are reported in Pavlinsky et al. (2019b). These included system effective area and vignetting measurements carried out at the IKI X-ray Test Facility.

Further calibration of the flight detector energy gain and resolution is done using the on-board ^{55}Fe + ^{241}Am sources (§ 8.4.1).

8.3   Operation

[[ ]grades, energy definition, resolution, PI,PHA (gain/thresholds); ground vs. on-orbit (particle background, background stability) sensitivity, background and background stability/variability]]

8.3.1   Event Registration

The process of event generation in the URD begins with a trigger pulse in the bottom strip with the highest pulse height amplitude (PHA) above a trigger threshold. The trigger threshold is unique to each strip. They have been set such that at least 50% of events with energies in the range 5-6 kEV are recognized as valid events. See Pavlinsky et al. (2019a) for details. The amplitude for the trigger strip and for the two adjacent strips are recorded into memory along with those of the information from the top strip with the largest amplitude above threshold and its two adjacent strips. A time stamp record is added to the event. The detector dead time is less than 0.8 ms. The event registration time error relative to the spacecraft time synchronization signals is less than 23 μs (Pavlinsky et al., 2021). This is

the basic observation mode. In this mode, the URD also periodically produces housekeeping frames that include, among other things, the detector temperature.[3] This information is sufficient to reconstruct the energy and detector coordinates of the event.

8.3.2   Event Energy Determination

First, the event is assigned a grade that is recorded as column GRADE in the event list. The grade describes the combination of the six recorded PHA values above a threshold as defined in Table 2. Events that only trigger a single strip in each layer have a GRADE value of 0 and are referred to as "singles". Events that trigger two strips in one or both layers have GRADE values of 1-8 depending on the precise pattern of strips triggered and are referred to as "doubles". Events that trigger all three strips in one or both layers (aka "triples") have GRADE values of 9-15. The vast majority of triple events originate from interactions of charged particles with the detector and generally should be excluded from any science analysis.

Second, the event energy is derived from a weighted combination of those among the six PHAs above threshold. The PHA-to-ENERGY scaling is a quadratic function,

$$E = c_o + c_1 PHA + c_2 PHA^2$$

where the coefficients, c_i are themselves linear functions of the detector temperature, T, and, of course, are unique to each electrode strip. Since both bottom and top layers provide independent information for the recorded event, a weighted linear combination of the top and bottom energy is made to minimize dispersion. For "singles":

$$E = \frac{\sigma_{\text{top}}^2}{\sigma_{\text{top}}^2 + \sigma_{\text{bot}}^2} E_{\text{bot}} + \frac{\sigma_{\text{bot}}^2}{\sigma_{\text{top}}^2 + \sigma_{\text{bot}}^2} E_{\text{top}}$$

where E_{bot} is scaled from the PHA in the central (trigger) electrode in the bottom layer and σ_{bot} is the standard deviation of the event PHA (as measured in ground calibration) and similarly for E_{top} and σ_{top}. For events with higher GRADES, similar averaging is applied (e.g., E_{bot} is a weighted average of the central and one or two adjacent strips) as described in the document MSFC-GAIN-D29-V00.pdf. All coefficients are archived in the ART-XC CALDB.

Table 2: Event GRADE Definitions[†]

GRADE	Top	Bot	GRADE	Top	Bot
0	OXO	OXO	8	OXX	OXX
1	XXO	OXO	9	XXX	OXO
2	OXX	OXO	10	XXX	XXO
3	OXO	XXO	11	XXX	OXX
4	OXO	OXX	12	OXO	XXX
5	XXO	XXO	13	XXO	XXX
6	XXO	OXX	14	OXX	XXX
7	OXX	XXO	15	XXX	XXX

[†]X denotes above PHA threshold, O denotes below threshold

8.3.3   Event Location Flags

As described in § 8.1, events recorded in the corners of the detectors occur underneath significant mechanical shielding by housing structure and are therefore unlikely valid (focussed) X-ray events. Rather, they are generated by energetic charged particles interacting with passive structures surrounding the detectors. Furthermore events recorded in any of the edge strips (top or bottom) do not have a full

---

[3]The thermal environment of the detectors has remained within -22 C to -19 C and is stable to ± 0.2 C per month.

complement of 6 PHA values for energy determination. Therefore, a status FLAG is defined for each event. Events in pixels located under the mechanical shielding are assigned a FLAG value of 2. Events in pixels along the outer boundaries of the detector, strip values 0 or 47 in either the top or bottom electrode layer, are assigned FLAG=3. The FLAG=3 strips typically have high count rates for reasons under study. All other events in the remaining locations on the detector are assigned FLAG=0. These events are visible to the sky and therefore should be included in any scientific analysis of an astrophysical source. The FLAG=2 regions differ among the seven detectors due to the offset orientations between the detectors and their Be windows. Thus, maps of distribution of FLAG values in detector coordinates are contained in the ART-XC CALDB and these FLAG values are assigned to each event in the final event list files.

8.4   Performance

[[spectra, timing, imaging; inputs to arf and rmf]]

8.4.1   Energy Scale and Resolution

[[here is where we discuss the ECS and show a spectrum or several (singles, doubles, triples, say)]]
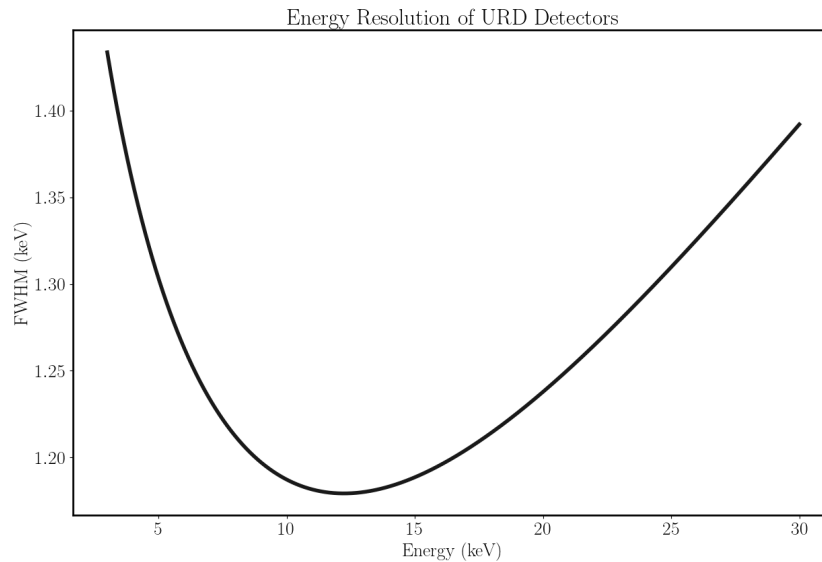

Figure 12:   The Full-Width at Half Maximum (FWHM) of the URD detectors as a function of energy in keV

9   Telescope Alignment and Aspect Solution

The ART-XC event list includes the detector pixel coordinate of each event (RAWX and RAWY). These detector coordinates can be written into the three dimensional, physical ART-XC module coordinate system, X, Y, and Z, defined as the following and illustrated in Fig. 2: the X axis passes through the geometric center of the detector and the center of the mirror module, the Y axis is defined as the direction opposite to the bottom side of the detector (i.e., along the negative RAWX direction), the Z axis is defined as the direction along the top side of the detector (i.e., along the RAWY direction). In practice, the origin of the detector coordinate with $RAWX = 0, RAWY = 0$ would be at $[y, z] = [24, -24] \times 0.595$mm. The X value of this point is 2693mm, which is identical to the focal length of the mirror module as the origin of the physical ART-XC module coordinate is at the top of the mirror module.

9.1   Alignment

The nominal X axis (§ 4) is not precisely coincident with the optical axis of the mirror modules. The optical axis positions are calibrated using in-flight observations of the Crab nebula consist of a series of snapshots with the Crab nebula at a range of off-axis angles and azimuthal positions. The optical axis position for each mirror module is defined as the center of a 2D Gaussian function of the Crab's count rate from snapshots at different off-axis and azimuthal angles. Table 3 lists the in-flight calibrated locations of the optical axis intersections in the Y, Z plane in detector (RAWX, RAWY) coordinates.

Table 3: ART-XC Telescope Optical Axes

Telescope	RAWX	RAWY	Telescope	RAWX	RAWY
T1	20.10	21.82	T5	21.37	19.71
T2	16.72	19.65	T6	21.57	22.16
T3	19.60	19.18	T7	19.72	21.92
T4	19.61	21.06			

9.2   Aspect Solution

The aspect solution for ART-XC is based on the the orientation data from the inertial navigation system (GYRO). The orientation data as a function of time is stored as tables of quaternion tensors. The equatorial coordinates corresponding to the detector plane can be derived via a quaternion rotation from the GYRO quaternions. However, before applying the quaternion operation, the GYRO quaternions requires an additional correctional quaternion term unique to each detector to account for the small but non-negligible offsets between different detector planes. To apply the quaternion operation, an event with detector coordinate RAWX and RAWY is re-written as a vector in the physical coordinates v_{XYZ} (see the first paragraph of this section for the definition of the ART-XC physical coordinate system), and the equatorial coordinate vector v_{J2000} can be obtained with the following equation:

$$v_{\mathrm{J2000}} = Q_{\mathrm{GYRO}} Q_{\mathrm{Corr}} v_{\mathrm{XYZ}}, \tag{1}$$

where Q_{GYRO} represents the GYRO quaternion tensor, and Q_{Corr} is the mirror-module-specific correctional quaterinon term. Note that the time resolution of the GYRO quaternion tensors is 1 second. As such, the Q_{GYRO} term in this equation is interpolated at the event arrival time. For the pointed-mode observations, the telescope pointing is stable by definition and hence no interpolation is needed. In the ART-XC data analysis software, the construction of v_{XYZ} includes a pixel-randomization step which randomize the RAWX and RAWY values within ± 0.5 pixel from the original integer values when converting to v_{XYZ}. This avoids the event equatorial coordinate values being "pixelized" and creating artificial structures in the X-ray images.

10   All-sky Survey

10.1   Tiling and WCS Projection

The SRG survey is divided into 4700 "tiles" covering the full sky. Each tile spans three degrees in declination and a range in right ascension such that each tile subtends a ≈ 8.78 square degree region on the sky. By default, the ART-XC data follows the tile definition of the SRG survey, which is included in the CALDB. As a part of ART-XC data processing pipeline, a FITS World Coordinate System (WCS) with a tangent projection is defined using the equatorial coordinates derived from aspect solutions. The sky coordinates defined by the WCS projection has a default 15″ square pixel size, and the central WCS coordinates of the projection are those of the tile center.

10.2

Stuff unique to the sky survey not covered elsewhere...

have already captured the survey pattern and exposure (briefly) and the variable arf (vignetting) and psf (size) vs off-axis angle. Here, then want to quantify the net effect (average/effective psf, say or avg. arf).

sensitivity: there is a figure in sunyaev.

References

Gubarev M., et al., 2012, in Takahashi T., Murray S. S., den Herder J.-W. A., eds, Society of Photo-Optical Instrumentation Engineers (SPIE) Conference Series Vol. 8443, Space Telescopes and Instrumentation 2012: Ultraviolet to Gamma Ray. p. 84431U, doi:10.1117/12.926207

Gubarev M., et al., 2014, in Takahashi T., den Herder J.-W. A., Bautz M., eds, Society of Photo-Optical Instrumentation Engineers (SPIE) Conference Series Vol. 9144, Space Telescopes and Instrumentation 2014: Ultraviolet to Gamma Ray. p. 91444U, doi:10.1117/12.2056595

Krivonos R., et al., 2017, Experimental Astronomy, 44, 147

Levin V., Pavlinsky M., Akimov V., Kuznetsova M., Rotin A., Krivchenko A., Lapshov I., Oleinikov V., 2014, in Takahashi T., den Herder J.-W. A., Bautz M., eds, Society of Photo-Optical Instrumentation Engineers (SPIE) Conference Series Vol. 9144, Space Telescopes and Instrumentation 2014: Ultraviolet to Gamma Ray. p. 914413, doi:10.1117/12.2056311

Levin V., Pavlinsky M., Akimov V., Kuznetsova M., Rotin A., Krivchenko A., Lapshov I., Oleynikov V., 2016, in den Herder J.-W. A., Takahashi T., Bautz M., eds, Society of Photo-Optical Instrumentation Engineers (SPIE) Conference Series Vol. 9905, Space Telescopes and Instrumentation 2016: Ultraviolet to Gamma Ray. p. 990551, doi:10.1117/12.2233324

Pavlinsky M., et al., 2018, Experimental Astronomy, 45, 315

Pavlinsky M., et al., 2019a, Experimental Astronomy, 47, 1

Pavlinsky M., et al., 2019b, Experimental Astronomy, 48, 233

Pavlinsky M., et al., 2021, A&A, 650, A42

Sunyaev R., et al., 2021, arXiv e-prints, p. arXiv:2104.13267

List of Acronyms

ART-XC	Astronomical Röntgen Telescope - X-ray Concentrator
BOKZ-MF	ART-XC Star-tracking Camera
CALDB	Calibration Database
eROSITA	extended ROentgen Survey with an Imaging Telescope Array
FOV	Field of View
FITS	Flexible Image Transport System
GSFC	Goddard Space Flight Center
HEASARC	High Energy Astrophysics Science Archive Research Center
HPD	Half Power Diameter
IKI	Russian Space Research Institute
MMA	Mirror Module Assembly
MOC	Mission Operations Center
MSFC	Marshall Space Flight Center

NPOL	Lavochkin Scientific and Production Association (Lavochkin Association)
OGIP	Office of General Investigator Programs
PHA	Pulse Height Amplitude
PSF	Point Spread Function
SLTF	Stray Light Test Facility
SRG	Spectrum-Röntgen-Gamma
URD	Unit of Röntgen Detector